ORIGINAL ARTICLE

$Ni_2As_2O_7$ pyrochlore nanomaterial: Solid state synthesis, crystal structure determination, crystal phase growth study and physical properties

Alireza Hakimyfard[*]

Department of Basic Science, Jundi-Shapur University of Technology, Dezful, Iran

Abstract

Nanostructured $Ni_2As_2O_7$ semiconductor samples were synthesized by a solid state method among As_2O_3 and $Ni(NO_3)_2.6H_2O$ raw materials at 650 °C (S_1) and 750 °C (S_2) as reaction temperatures. The synthesized nanomaterials were characterized by powder X-ray Diffraction (PXRD) technique and Fourier-Transform Infrared (FTIR) spectroscopy. The Rietveld analysis showed that the obtained materials were crystallized well in the triclinic crystal structure with the space group P_1. The data of Rietveld analysis showed that the purity of the synthesized nanomaterials was increased by increasing the reaction temperature. The morphologies of the synthesized materials were studied by field emission scanning electron microscope (FESEM). It was found that the morphology of the obtained materials was changed from homogeneous sponge to particles and somewhat porous structure, by increasing the reaction temperature. Besides, the average particle sizes were increased considerably by increasing the reaction temperature. Ultraviolet-visible spectra analysis showed that the synthesized $Ni_2As_2O_7$ nanomaterials had strong light absorption in the ultraviolet light region. The direct optical band gap energies were 3.20, 3.90, 4.80 eV and 2.9, 3.40, 4.70 eV for S_1 and S_2, respectively. The data showed that the band gaps were decreased by increasing the reaction temperature that can be due to the increasing the crystallite sizes of the targets.

Keywords: *$Ni_2As_2O_7$; Pyrochlore; Rietveld; Semiconductor; Solid State Method.*

INTRODUCTION

Pyrochlore materials with the general formula of $A_2B_2O_7$ (where A is a medium-large cation and B is an octahedrally coordinated, high charge cation) have been widely studied for their technological potential applications. Here the A/B cations can be either in the +2/+5 oxidation state [1-3]. $A_2B_2O_7$ pyrochlore materials have attracted great interest due to their ability to form substituted and defective structures, allowing interesting physical properties [4-5]. Furthermore, $A_2B_2O_7$ pyrochlore materials have drawn attention for applications such as immobilization of fission products [6], catalysis [7–13], and solid electrolytes [14]. Alkaline earth arsenates (V) are of interest in many different research areas and have been the subject of several previous studies [15-17]. The $Ni_2As_2O_7$ is composed of Ni(II) and As(V) cations which

make NiO and As_2O_5 metal oxides structures in the pyrochlore crystal system. The properties of the metal oxides have been studied numerously. Nickel (II) oxide has been receiving considerable attention due to its electrical, magnetic and catalytic properties. Its wide range of applications in various fields included the fabrication of catalysts, electrochromic films, fuel cell electrodes and gas sensors, battery cathodes, P-N heterojunctions, magnetic materials, photovoltaic devices, electrochemical supercapacitors, smart windows and dye-sensitized photocathodes [18-27]. Arsenic (III) trioxide is the precursor to elemental arsenic, arsenic alloys, and arsenide semiconductors. Organoarsenic compounds and bulk arsenic-based compounds are derived from arsenic trioxide. A variety of applications exploit arsenic's toxicity, including the use of the oxide

* Corresponding Author Email: *ahakimyfard@jsu.ac.ir*

as a wood preservative [28, 29]. It has been shown that arsenic trioxide induces cancer cells to undergo apoptosis. Due to the toxic nature of arsenic, this carries significant risks [30, 31]. There are two reported methods for the synthesis of $Ni_2As_2O_7$ including chemical transport reaction [32], heat treatment of As_2O_3 and NiO at different reaction temperatures [33].

To the best of our knowledge, there is no report on the synthesis of the targets with the introduced conditions (raw material type, and reaction time and temperature) in the present study. For the purpose, a solid state route is applied to synthesize nanostructured $Ni_2As_2O_7$ powders using As_2O_3 and $Ni(NO_3)_2$. The Rietveld analysis is used for the characterization and study of the crystalline phase growth and purity of the obtained materials. FESEM and BET-BJH analyses are used for investigating the physical properties of the obtained nanomaterials. The direct optical band gap energies are calculated and related to the reaction temperature and crystalline sizes of the obtained semiconductor nanomaterials.

EXPERIMENTAL
Materials and instruments
All chemicals including As_2O_3 and $Ni(NO_3)_2.6H_2O$ were of analytical grade and were obtained from commercial sources (Merck Company) and used without further purifications. Phase identifications were performed on a powder X-ray diffractometer D5000 (Siemens AG, Munich, Germany) using CuK_α radiation. The Rietveld analysis was done by FullProf software. The morphology of the obtained materials was examined with a field emission scanning electron microscope (Hitachi FE-SEM model S-4160). The surface area and pore volume and average nanoparticles size were calculated using the Brunauer-Emmett-Teller (BET) equation. Pore size distributions, pore volume and pore surface area were calculated by the Barrett-Joyner-Halenda (BJH) method. BET surface areas were acquired on a Beckman Coulter SA3100 Surface Area Analyzer. FTIR spectrum was recorded on a Tensor 27 (Bruker Corporation, Germany). The average of particle size distribution was carried out using Image software. Absorption spectra were recorded on a UV-visible spectrophotometer model-UV-1650 PC (Shimadzu, Japan).

Solid state synthesis of $Ni_2As_2O_7$ nanopowders
In a typical experiment for the synthesis of S_1,

0.291 g (1 mmol) of $Ni(NO_3)_2.6H_2O$ (Mw = 290.7 g mol^{-1}) and 0.198 g (1 mmol) of As_2O_3 (Mw = 197.87 g mol^{-1}) were mixed in a mortar and ground until a homogeneous powder was obtained. The obtained powder was added to a 25 mL crucible and treated thermally in one step in a furnace at 650 °C (S_1) and 750 °C (S_2) for 8 h. The crucible was then cooled normally in the furnace to the room temperature. The obtained yellow powder was collected for further analyses. The synthesis yields for $Ni_2As_2O_7$ (Mw= 267.22 g mol^{-1}) were 0.21 g (79 %) and 0.24 g (90 %) for S_1 and S_2, respectively.

RESULTS AND DISCUSSIONS
Characterization
The X-ray diffraction patterns of the $Ni_2As_2O_7$ samples are reported in Fig. 1(a and b) as data points, together with the result of the profile matching analysis (full lines) in the θ-2θ geometry with Cu-Kα radiation. Structural analysis was done by the *FullProf* program by employing profile matching with constant scale factor. The results shown in Fig. 1 a shows that small amount of As_2O_3 as impurity phase was detected for S_1 with a space group $P12_1/a1$ denoted by red bars in Fig. 1a [28, 29]. The lattice parameters of the impurity phase were found as a= 12.53 Å, b=4.35 Å, and c=16.53 Å with α=γ=90 and β=143.04°. However, Fig. 1b indicates that there is no impurity phase in the obtained target. It was found from Fig. 1(a and b) that the patterns had a main $Ni_2As_2O_7$ crystal structure with space group P_1 (JCPDS number: 10-0326). The peak positions at 2θ = 17.45, 20.96, 28.33, 28.83, 30.25, 35.10, 35.60, 37.20, 37.95, 39.20, 41.29, 42.80, 44.03, 45.98, 47.07, 48.32, 53.36, 54.43, 55.52, 56.52, 58.20, 59.11, 60.96, 61.70, 66.48, 67.48, 71.25, 74.93, 79.11, 82.46, 85.90 ° are indexed to the h k l values = -3 0 1, 0 1 0, 3 0 0, -2 1 2, -6 1 3, -3 2 1, -5 0 3, -6 2 3, -6 1 1, 0 0 2, -4 -1 1, 0 2 0, -9 1 3, 2 1 1, 0 2 1, -7 0 4, -6 -1 3, 6 -1 0, 3 1 1, -5 3 1, -12 2 4, -3 -2 2, 3 2 0, -4 3 3, 0 3 0, -9 2 6, -5 -2 3, -6 4 3, -14 1 6, -9 4 2, -8 4 5, -6 2 6, respectively. The lattice parameters were found as   a = 19.54 Å, b = 5.30 Å, and c = 8.89 Å with α=58.28, β= 148.84° and γ=127.33° [32, 33].

The quantitative phase analysis was investigated by the direct comparison method. In this method, we compared the experimental line intensity of the impurity phase (As_2O_3) from the mixture to a line from the main phase ($Ni_2As_2O_7$) in the mixture. For this purpose, we chose the peaks with the highest intensity for each phase

at about 26.8˚ and 28.5˚ for As_2O_3 and $Ni_2As_2O_7$, respectively. The phase comparison values are summarized in Table 1. Table 1 shows that the purity of the obtained $Ni_2As_2O_7$ nanomaterials is 84 and 100 % for S_1 and S_2, respectively. It shows that the reaction temperature is a main factor in the crystalline phase purity. Besides, the counts values are included in Table 1. The data shows that the crystal phase growth values of the targets are related considerably to the reaction temperature. It indicates that the obtained materials are crystallized better when the reaction temperature is increased from 650 to 750 °C.

Table 2 shows the interplanar spacing (d) calculated from Bragg's equation and the lattice parameters data obtained from Rietveld analyses for S_1 and S_2, respectively. It was found that the d

and lattice parameters values were increased by increasing the reaction temperature. According to the data, it can be concluded that the volume of the unit cell is increased by increasing the reaction temperature.

Table 3 shows the crystallite sizes of the as-synthesized nanomaterials calculated by Scherrer equation:

$$\cos\theta = \frac{K\lambda}{D} \cdot \frac{1}{B_{\frac{1}{2}}} \tag{1}$$

In the equation, D is the entire thickness of the crystalline sample, λ is the *X-ray* diffraction wavelength (0.154 nm), and k is the Scherrer constant (0.9), $B_{1/2}$ of FWHM is the full width at half its maximum intensity and θ is the half diffraction angle at which the peak is located. For the
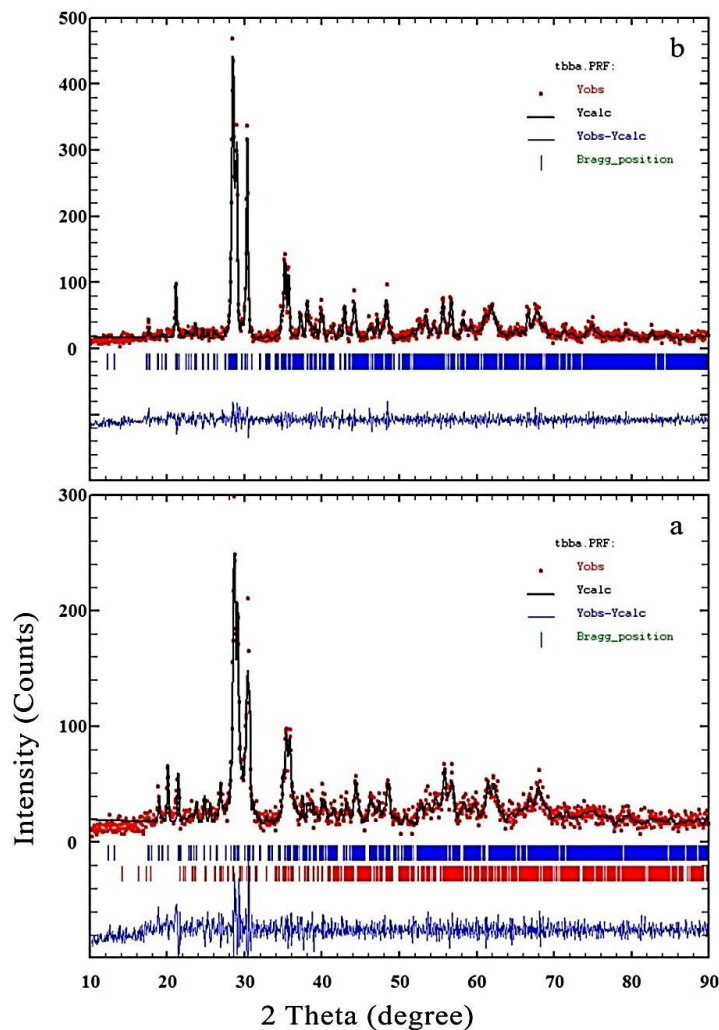

Fig. 1: Powder X-Ray diffraction patterns and the Rietveld analyses of a) S_1 and b) S_2.

Table 1: Quantitative phase analyses for the obtained nanomaterials.

Sample	Rietveld parameters			$Ni_2As_2O_7$ Phase purity (%)	Counts
	R_{Bragg}	R_f	χ^2		
S_1	2.49	1.04	1.54	84	298
S_2	1.61	1.10	1.29	100	468

Table 2: Interplanar spacing (d) and cell parameters data for $Ni_2As_2O_7$ nanomaterials.

Sample	d (Å)	a (Å)	b (Å)	c (Å)	Vol (Å³)
S_1	3.108	19.27596	5.21423	8.82107	887
S_2	3.132	19.54064	5.29919	8.89026	921

purpose, we used the above equation to calculate the crystallite size of the samples. The data indicates that the crystallite size of the synthesized nanomaterials were increased from 28 to 32 nm with increasing the reaction temperature from 650 to 750°C. The value of the dislocation density (δ) which is related to the number of defects in the crystal was calculated from the average values of the grain size (D) by the relationship given below:

$$\delta = \frac{1}{D^2} \qquad (2)$$

The data of the dislocation values are summarized in Table 3. The behavior of decreasing the dislocation density mentioned in the table is due to the increasing the crystalline sizes of the materials obtained by changing the reaction temperature.

The strain (ε) values were also determined by the use of the following formula:

$$\varepsilon = \frac{\beta_{hkl}\, cos\theta}{4} \qquad (3)$$

The variation in the strain as a function of synthesis reaction conditions is included in Table 3. The decreasing in the strain values is probably due to the improvement in the degree of crystalline of the obtained crystals. So, the data indicate that the synthesis reaction conditions influence the crystallite size, strain and dislocation density values.

Morphology Analysis

Fig. (2 and 3) show the FESEM images of S_1 and S_2, respectively. Fig. 2(a and b) show that the morphology of the obtained material is the sponge. Besides, Fig. 2c and 2d show that, the particle size and morphology of the target is homogeneous. However, Fig. 3(a and 3b) show that the material is composed of particles and porous structures. It is clear that the porosity of the material is smaller than that of S_1. Fig. 3(c and d) shows that the particle size of the target is nearly heterogeneous. Fig. 4a shows the particle size distribution profile of the S_1. It shows that the maximum particle size distribution is in the range of 50–60 nm. Besides, Fig. 4b shows the particle size distribution profile of S_2. It indicates that the maximum particle size distribution is in the ranges of 80 – 90 and 100–110 nm. The data of the particle size distribution profiles obtained from the FESEM images show that the particle sizes of the targets are increased by increasing the reaction temperature from 650 to 750 °C. This conclusion is in agreement with the crystallite size data of the targets calculated by Scherrer equation. Besides, the volume of the unit cell obtained from Rietveld analysis showed that the value was increased with increasing the reaction temperature. It is in a good agreement with that of the data obtained from the particle size distribution data.

Table 3: Scherrer data information for $Ni_2As_2O_7$ nanomaterials.

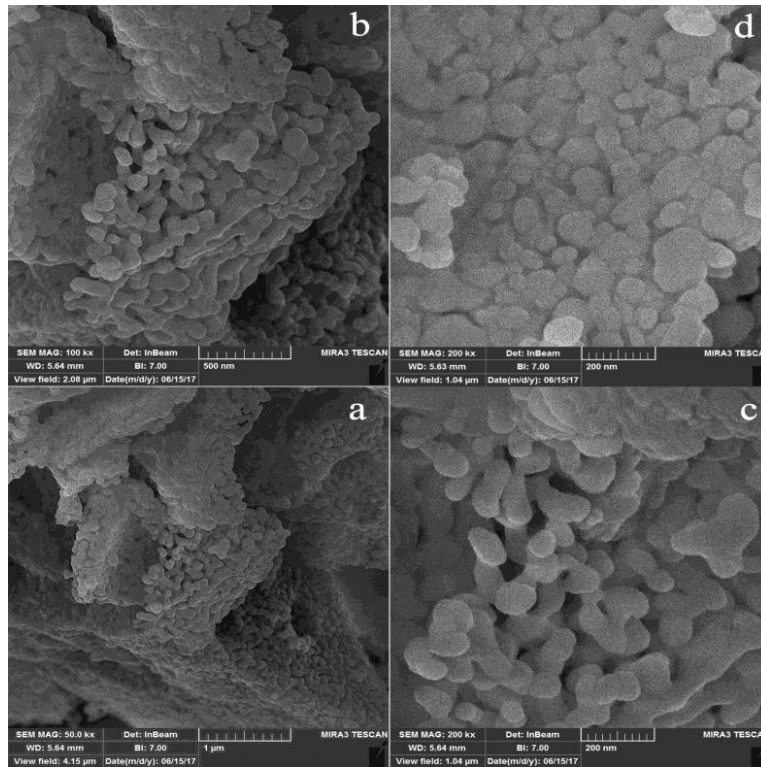| Sample	2θ	θ value	$B_{1/2}$ (°)	$B_{1/2}$ (rad)	$cos\theta_B$	D (nm)	δ(lines/m²) × 10¹⁴	ε× 10⁻³
S_1	28.4948	14.2474	0.28856	0.00503377	0.969242	28	12.8	4.8
S_2	28.4643	14.23215	0.25793	0.00449945	0.969308	32	9.7	4.4

Fig. 2: FESEM images of S1 where a and b indicate the sponge morphology, c and d shows the homogeneity of size and morphology.
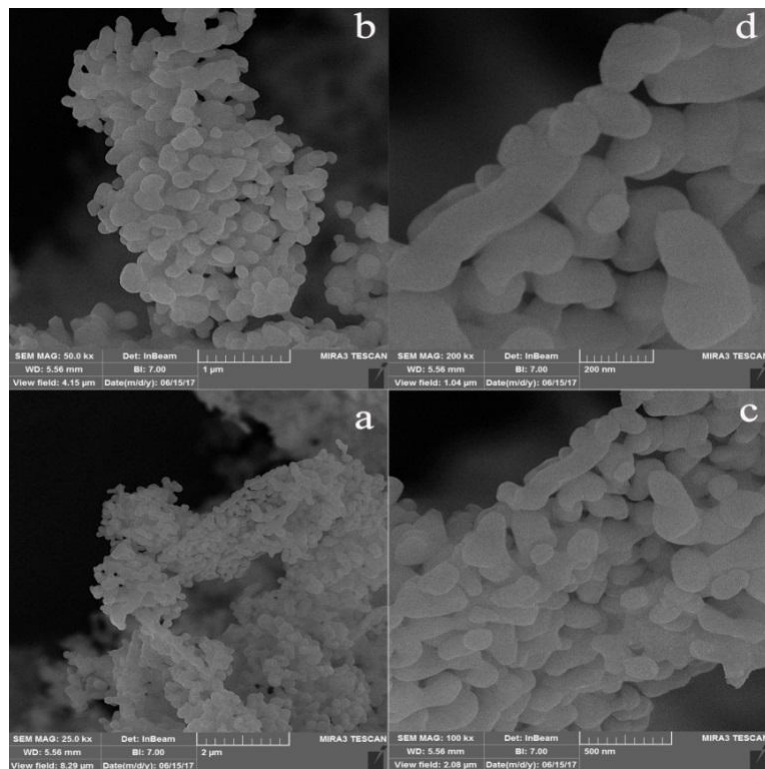

Fig. 3:FESEM images of S$_2$ where a and b shows the porous structure, c and d shows the morphology and homogeneity of the particles.

BET and BJH texture analysis

The synthesized powders were characterized by their surface area, average pore size and average pore volume. Prior to N_2-physical adsorption measurement, the samples were degassed at 150 °C for 120 min in the nitrogen atmosphere. So, the specific surface area (S_{BET}) of the obtained materials was determined with adsorption-desorption isotherms of N_2 at 77 K. The surface area, pore volume and average pore diameter of

Table 4: BET data for $Ni_2As_2O_7$ showing the textural properties of the obtained materials.

Sample	BET surface area (m^2g^{-1})	Pore diameter (nm)	Pore volume (cm^3g^{-1})
S_1	11.321	54	0.153
S_2	5.0985	19	0.0245

Table 5. BJH data for $Ni_2As_2O_7$ showing the textural properties of the obtained materials.

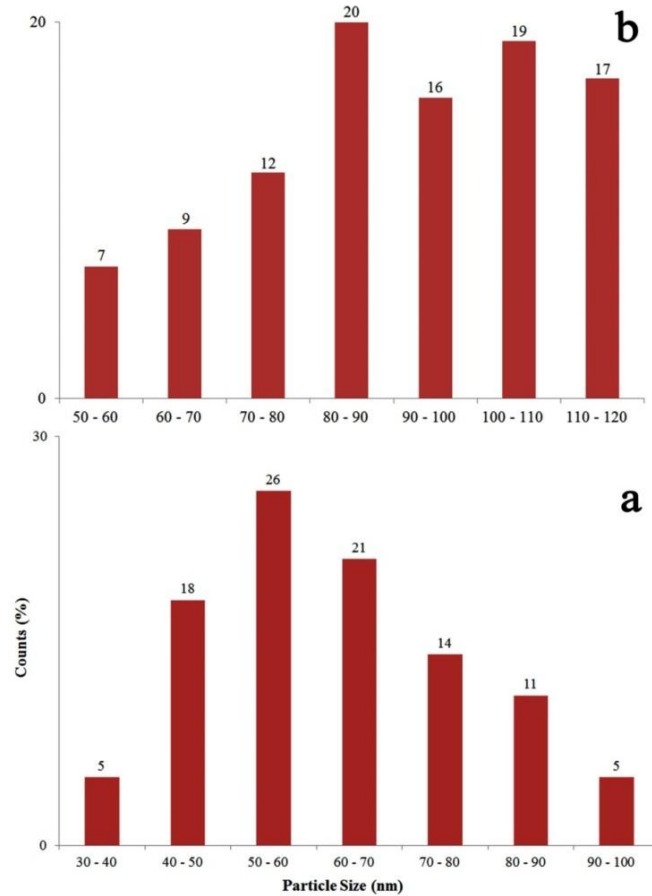| Property	S_1	S_2
BJH adsorption cumulative surface area of pores	12.713	6.008
BJH adsorption cumulative volume of pores	0.154	0.0251
BJH adsorption average pore width (4V/A)	48	17

Fig. 4: Particle size distribution profiles of a) S_1 and b) S_2.
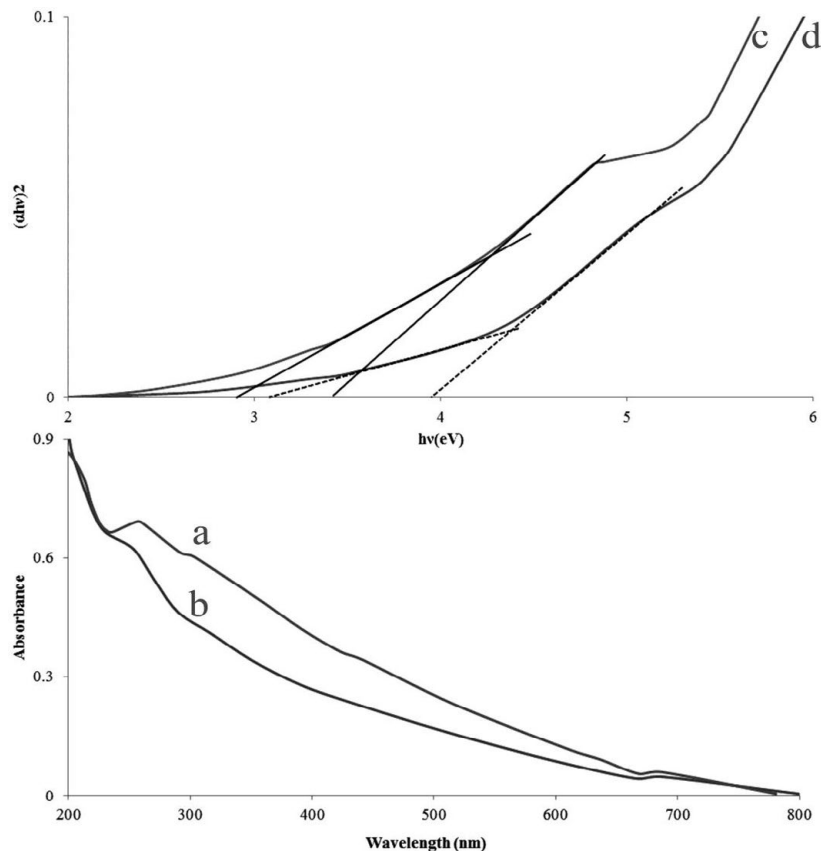
Fig. 5: UV-Vis spectra of a) S1 and b) S_2; plots of $(\alpha h\nu)2$ versus $h\nu$ (eV) of c) S_1 and d) S_2.

the synthesized materials are summarized in Table 4. From Table 4, it can be seen that the specific surface area and pore volumes are 54 m²g⁻¹ and 19 cm³ g⁻¹ for S_1, 0.153 and 0.0245 cm³g⁻¹ for S_2, respectively. Also, for samples S_1 and S_2, the average pore diameter sizes were measured as 54 and 19 nm, respectively. Table 5 shows the textural properties of the as-prepared materials obtained from BJH analysis. The data summarized in Table 5 shows that the specific surface area of the pores, pore width and pore volume of S_2 is smaller than that of S_1. So, the investigated results of BET and BJH measurements suggest that the surface area, average pore diameter sizes and average pore volume of S_2 is smaller than that of S_1 with increasing the reaction temperature from 650 to 750 °C. The decreasing the specific surface area and pore volume values of the targets with increasing the reaction temperature is in good agreement with the data obtained from the FESEM images and particle size distribution data (Figs. 2 and 3).

Optical Properties

The UV-Vis absorption spectra (a, b) of the $Ni_2As_2O_7$ semiconductor nanomaterials and direct band gaps (c, d) are shown in Fig. 5a-d. According to the results of Pascual *et al.* [34], the relation between the absorption coefficient and incident photon energy can be written as $(\alpha h\nu)^2 = A(h\nu - E_g)$, where A and E_g are a constant and the direct band gap energy, respectively. The bandgap energies were evaluated by extrapolating the linear part of the curves to the energy axis. The direct optical band gaps were 3.20, 3.90, 4.80 eV and 2.9, 3.40, 4.70 eV for S_1 and S_2, respectively. The decreasing the band gap energies could be attributed to the increasing the particle sizes of the obtained materials.Fig. 6(a and b) shows the FTIR spectra of S_1 and S_2. There are some peaks at around 450, 495, 515, 600, 744, 833, 862, 993 and 1394 cm⁻¹. The strong bands at 450, 495, 515 cm⁻¹ are assigned to the As–$O_{bridging}$ stretches. The band at about 744 cm⁻¹ is attributed to the symmetric As–$O_{terminal}$ stretches. The band at around 833
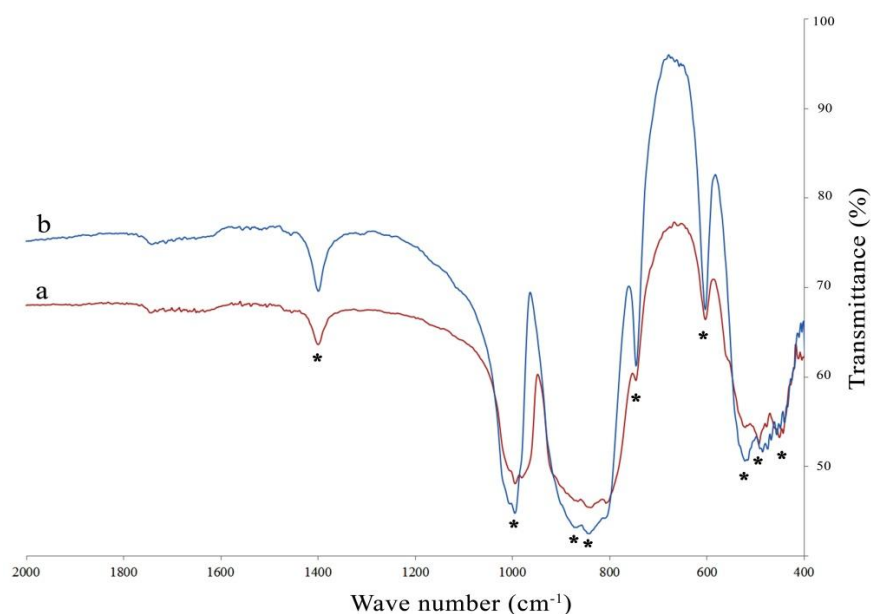
Fig. 6: FTIR spectra of a) S_1 and b) S_2.

cm^{-1} is assigned to doubly degenerate stretching vibrations of As-O bonds [35-37].

CONCLUSION

In this work, $Ni_2As_2O_7$ nanomaterials were synthesized by solid state method. PXRD patterns and structural analysis done by the *FullProf* program employing profile matching showed that the synthesis procedures were sucsessful. The Rietveld analysis showed that the obtained materials were crystallized in a triclinic crystal system. The purity of the targets were also studied by the direct comparison method using the PXRD patterns. The data showed that the phase purity and crystal phase growth values were increased by increasing the reaction temperature. FESEM images showed the morphologies of the targets were the sponge for S_1 and somewhat porous for S_2. So it indicated that the specific surface areas and pore volumes of the materials were decreased. It is in agreement with the FESEM images. It was found that the morphology of the obtained materials was changed and the particle size distributions of the targets were increased by increasing the reaction temperature. Also, the direct optical band gaps were calculated and related to the reaction temperature. The data that the band gaps were decreased by increasing the reaction temperature from 650 °C to 750 °C.

CONFLICT OF INTEREST

The authors declare that there is no conflict of interests regarding the publication of this manuscript.

REFERENCE

[1] Sellami M., Caignaert V., Hamdad M., Belarbi A., Sari-Mohamed I., Bahmani A., Bettahar N., (2011), Synthesis and characterization of the new pyrochlore $Bi_{1.5}Sb_{1.5-x}Nb_xMnO_7$ solid solution. *C. R. Chim.* 14: 887-890.

[2] Khademinia S., Behzad M., Jahromi H. S., (2015), Catalytic performance of bismuth pyromanganate nanocatalyst for Biginelli reactions. *RSC. Adv.* 5: 24313-24318.

[3] Khademinia S., Behzad M., (2015), Low temperature hydrothermal synthesis, characterization and optical properties of strontium pyroniobate. *Adv. Powder. Technol.* 26: 644-649.

[4] Khademinia S., Behzad M., (2015), Lanthanum cerate ($La_2Ce_2O_7$): hydrothermal synthesis, characterization and optical properties. *Int. Nano Lett.* 5: 101-107.

[5] Khademinia S., Behzad M., (2015), Bismuth Pyromangenate: Hydrothermal and solid state synthesis, characterization and optical properties. *J. Adv. Mater. Proc.* 3: 77-84.

[6] Pirzada M., Grimes R. W., Maguire J., Sickafus K., (2002), Select Predictions of strontium accommodation in $A_2B_2O_7$ pyrochlores. *J. Mater. Res.* 17: 2041-2047.

[7] Cheng J., Li J., Ma C., Hao Z., (2009), Catalytic combustion of methane over $La_2TM_{0.3}Zr_{1.7}O_{7-\delta}$ (TM = Mn, Fe, and Co) pyrochlore oxides. *Catal. Commun.* 10: 1170-1173.

[8] Christopher J., Swamy C. S., (1991), Surface characterization and catalytic activity of $Ln_2Ti_2O_7$ (Ln=Y, Sm, Gd and Tb). *J. Mater. Sci.* 26: 4966-4970.

[9] Haynes D. J., Berry D. A., Shekhawat D., Gardner T. H., Spivey J. J., (2007), Catalytic partial oxidation of n-tetradecane on Rh- and Sr-substituted pyrochlores. *Am. Chem. Soc. (ACS)*

Division of Energy and Fuels. 52: 284-285.

[10] Haynes D. J., Berry D. A., Shekhawat D., Spivey J. J., (2009), Catalytic partial oxidation of n-tetradecane using Rh and Sr substituted pyrochlores: Effects of sulfur. *Catal. Today.* 145: 121-126.

[11] Park S., Hwang H. J., Moon J., (2003), Catalytic combustion of methane over rare earth stannate pyrochlore. *Catal. Lett*. 87: 219-223.

[12] Sohn J. M., Kim M. R., Woo S. I., (2003), The catalytic activity and surface characterization of $Ln_2B_2O_7$ (Ln=Sm, Eu, Gd and Tb; B=Ti or Zr) with pyrochlore structure as novel CH_4 combustion catalyst. *Catal. Today*. 83: 289-297.

[13] Jiang Z., Su J., Han Y., Alshahrani F., Hao Z., Xiao T., (2005), The effect of transition metal in Sn-based pyrochlores on the methane catalytic combustion. *Prog. Nat. Sci.* 15: 134-138.

[14] Wuensch B. J., Eberman K. W., Heremans C., Ku E. M., Onnerud P., Yeo E. M. E., Haile S. M., Stalick J. K., Jorgensen J. D. (2000), Connection between oxygen-ion conductivity of pyrochlore fuel-cell materials and structural change with composition and temperature. *Solid State Ionics*. 129: 111-133.

[15] Weil M., (2001), Cadmium (II) diarsenate (V), $Cd_2As_2O_7$. *Acta Cryst. E.* 57: 28-29.

[16] Harvey C. F., Ashfaque K. N., Yu W., Badruzzaman A. B. M., Ali M. A., Oates P. M., Michael H. A., Neumann R. B., Beckie R., Islam S., Ahmed M. F., (2006), Groundwater dynamics and arsenic contamination in Bangladesh. *Chem. Geol.* 228: 112-136.

[17] Raicevic S., Stanic V., Kaludjerovic-Radoicic T., (2007), Theoretical assessment of calcium arsenates stability: Application in the treatment of arsenic contaminated waste. *Mater. Sci. Forum.* 555: 131-136.

[18] Chrissanthopoulos A., Baskoutas S., Bouropoulos N., Dracopoulos V., Poulopoulos P., Yannopoulos S. N., (2011), Synthesis and characterization of ZnO/NiO p-n heterojunctions: ZnO nanorods grown on NiO thin film by thermal evaporation. *Photon. Nanostruc*. 9: 132-139.

[19] Wu Y., Wu G., Ni X., Zhou Z., Zhang H. Q., Wu X., (1999), Electrochromic characteristics of nickel oxide film in Li^+ containing electrolyte. *J. Inorg. Mater.* 14: 257-263.

[20] Ghosh M., Biswas K., Sundaresan A. C., Rao N. R., (2006), MnO and NiO nanoparticles: Synthesis and magnetic properties. *J. Mater. Chem.* 16: 106-111.

[21] Del Bianco L., Boscherini F., Tamisari M., Spizzo F., Vittori Antisari M., Piscopiello E., (2008), Exchange bias and interface structure in the Ni/NiO nanogranular system. *J. Phys. D.: Appl. Phys.* 41: 134008-134014.

[22] Ahmad T., Ramanujachary K. V., Lofland S. E., Ganguli A. K., (2006), Magnetic and electrochemical properties of nickel oxide nanoparticles obtained by the reverse-micellar route. *Solid State Sci.* 8: 425-430.

[23] El-Kemary M., Nagy N., El-Mehasse I., (2013), Nickel oxide nanoparticles: Synthesis and spectral studies of interactions with glucose. *Mater. Sci. Semicond. Process*. 16: 1747–1752.

[24] Rahdar A., Aliahmad M., Azizi Y., (2015), NiO nanoparticles: Synthesis and characterization. *J. Nanostruc.* 5: 145- 151.

[25] Riazian M., (2014), Synthesis and nano structural study on TiO_2-NiO-SiO_2 composite. *Int. J. Nano Dimens.* 5: 123-131.

[26] Zahraei F., Rahimi K., Yazdani A., (2015), Preparation and characterization of Graphene/Nickel oxide nanorods composite. *Int. J. Nano Dimens.* 6: 371-376.

[27] Khanahmadzadeh S., Barikan F., (2014), Fabrication and magnetic properties of Polyimide/Nickel Oxide nanocomposite. *Int. J. Nano Dimens.* 5: 365-370.

[28] Grund S. C., Hanusch K., Wolf H. U., (2005), Arsenic and arsenic compounds, ullmann's encyclopedia of industrial chemistry. Weinheim: Wiley-VCH, doi:10.1002/14356007. a03_113.pub2.

[29] Gibaud S., Jaouen G., (2010), Arsenic-based drugs: From fowler's solution to modern anticancer chemotherapy. *Top. Organomet. Chem.* 32: 1-20.

[30] Rao Y., Li R., Zhang D., (2013), A drug from poison: How the therapeutic effect of arsenic trioxide on acute promyelocytic leukemia was discovered. *Sci. China Life Sci.* 56: 495-502.

[31] Soignet S. L., Frankel S. R., Douer D., Tallman M. S., Kantarjian H., Calleja E., Stone R. M., Kalaycio M., Scheinberg D. A., (2001), United states multicenter study of arsenic trioxide in relapsed acute promyelocytic Leukemia. *J. Clin. Oncol*. 19: 3852-3860.

[32] Weil M., Stoger B., (2010), Crystal chemistry of transition metal diarsenates $M_2As_2O_7$ (M = Mn, Co, Ni, Zn): Variants of the thortveitite structure. *Acta Cryst. B.* 66: 603–614.

[33] Padmanabham A., Gandhi Y., Satyanarayana T., Veeraiah N., (2009), Spectroscopic and dielectric properties of crystallized $PbO–Sb_2O_3–As_2O_3$: NiO glass system. *J. Alloys Compd.* 488: 400-408.

[34] Pascual J., Camassel J., Mathieu M., (1978), Fine structure in the intrinsic absorption edge of TiO_2. *Phys. Rev. B: Solid State*. 18: 5606-5614.

[35] Bishay A., Maghrabi C., (1969), Properties of bismuth borate glasses in relation to structure. *Phys. Chem. Glasses*. 10: 1-11.

[36] Srinivisa Rao G., Veeraiah N., (2001), Study on various physical properties of $PbO–As_2O_3$ glasses containing manganese ions. *J. Alloys Compd*. 327: 52-56.

[37] Đorđević T., Wittwer A., Jagličić Z., Djerdj I., (2015), Hydrothermal synthesis of single crystal $CoAs_2O_4$ and $NiAs_2O_4$ compounds and their magnetic properties. *RSC Adv*. 5: 18280-18287.